Nanoscale

Accepted Manuscript

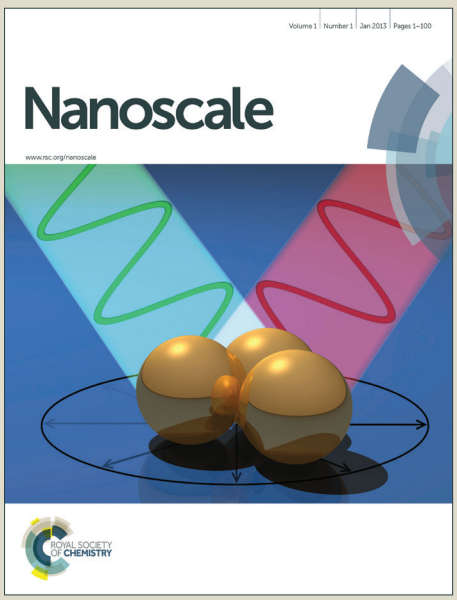

ROYAL SOCIETY OF CHEMISTRY

www.rsc.org/nanoscale

Journal Name

RSCPublishing

ARTICLE

New insight on optical and magnetic Fe_3O_4 nanoclusters promising for near infrared theranostic applications.

Cite this: DOI: 10.1039/xoxxoooooox

Received ooth January 2012,
Accepted ooth January 2012

DOI: 10.1039/xoxxoooooox

www.rsc.org/

Chih-Chia Huang [a,b,c*] Po-Yang Chang,[a,b] Chien-Liang Liu,[a] Jia-Pu Xu,[b] Shu-Pao Wu,[d] and Wen-Chuan Kuo, [b,c*]

Extensive efforts have been devoted to the development of a new biophotonic system using near-infrared (NIR) nanoagents for noninvasive cancer diagnosis and therapy. Here, we developed a simple synthesis reaction of ligands, hydrazine, and iron(II) chloride to fabricate Fe_3O_4 cluster-structured nanoparticles (CNPs) with interesting NIR photonics and high magnetization (M_s: 98.3 emu/g and proton relaxivity r_2: 234.6 $mM^{-1}s^{-1}$). These Fe_3O_4 CNPs exhibited optical absorption and reflection over all wavelengths, showing a U-shape absorption band with a low absorbance at a range of 750-950 nm and a progressive evolution in the second near-infrared region. The strengthening of the scattering effect by incubating Fe_3O_4 CNPs with HeLa cells performed optical contrast enhancement in optical coherence tomography (OCT) microscope system with a laser light source at 860 nm. A 1064 nm laser at a low power density (380 mW/cm^2) to excite the Fe_3O_4 CNPs (375 $ppm_{[Fe]}$) led to a rise in the water temperature from 25 °C to 58 °C within 10 min. Finally, we present the first example of magnetomotive OCT cellular imaging combined with enhanced photothermal therapy by using Fe_3O_4 CNPs and applying a magnetic field, which is promising for preclinical and clinical trials in the future.

1. Introduction

The developments of new Fe_3O_4 nanostructures and properties are emerging as promising agents for the selective and magnetic separation of various biological molecules as well as exploitation to aid in disease diagnosis, detection, and therapy treatment without invasive procedures.[1-4] As an example of the new concept of photomedicine and theranostics, it is desirable to develop a simultaneously near infrared (NIR)-activated and magnetic-functionalized nanoagents to treat cancer. Although engineering the shape of Au nanomaterials potentially provided an opportunity to tailor the surface plasmon resonance in the NIR wavelengths, the developed Au NIR-photoabsorbers did not combine with the magnetic features.[1] However, the optical properties of Fe_3O_4 nanoparticles were less explored and thus limited their photomedicine developments.

Based on the inverse spinel structured magnetite (Fe_3O_4) material, Fe(II) and Fe(III) in the octahedral sites of the crystal was found to produce an intervalence charge transfer (IVCT)[5,6] that gives rise to the second near-infrared (NIR-II) region at 1000-1350 nm. NIR laser radiation for reaction at the NIR-II wavelengths were less affected by scattering losses and capable of deeper penetration.[7] However, most Fe_3O_4 nanoparticles have had a nonstoichiometric structure and thus failed to increase the optical absorption band in the NIR wavelength regions.[5] Challenges still remained when control the oxidation states of ultra-small superparamagnetic iron oxide (USPIO) particles due to its air sensitivity. As the particle size becomes smaller, it is more likely to form maghemite.[8]

The aim of the work herein described was to develop integrated high-quality and NIR optical of iron oxide cluster-structured nanoparticles, referred to Fe_3O_4 CNPs, by a facile synthesis with hydrazine-assisted reduction and hydrothermal environment. A progressive evolution of absorption of Fe_3O_4 CNPs appeared in the NIR-II region to perform remarkable photothermal conversion feature (20.8%) induced by 1064 nm laser. A single particle consisted of several aggregated small particles promoted the magnetization up to 113 emu/$g_{[Fe]}$ and exhibited large proton relaxivity r_2 (234.6 $mM^{-1}s^{-1}$) in contrast to the previous results of Fe_3O_4 nanoparticles with hydrothermal reaction processes.[9] As a proof of concept of the magnetic and NIR-optical functions of Fe_3O_4 CNPs in biological treatments, medicine, we assessed, through in vitro studies, its ability to magnet-assisted photothermal ablation of cervical cancer line HeLa after treating with Fe_3O_4 CNPs and applying a NIR-II laser at 1064 nm (380 mW/cm^2). To the best of our knowledge, this study is the first to show photothermal cancer therapy of Fe_3O_4 nanoparticles in the second NIR window.[10-12] In additional, we utilized optical coherence tomography (OCT) by using an 860 nm laser (NIR-I regions: 650 nm - 950 nm) to demonstrate that the Fe_3O_4 CNPs-treated cells were visualized and moveable with a magnet control, showing a promising optical contrast agent for dynamic medical imaging.

OCT provides a higher resolution than ultrasonography, magnetic resonance imaging (MRI) or X-ray computed tomography (CT) and has a deeper imaging depth than confocal or multi-photon microscopy.[13,14] OCT with NIR laser provides noninvasive imaging modality.[15-17] This imaging system provides faster to construct bigger deep and large-area tissue imaging than using fluorescent imaging method. As the scattering cross-section does not vary widely between molecular species, OCT is still limited to nonspecific material properties without contrast agents.[18] In recent years, dyes,[19-21] gold,[22,23] and organic polymer nanoparticles[24]

have been suggested as potential NIR OCT contrast agents. Nonetheless, these reagents did not supply high magnetization for additional magnetic functions and magnetic guided delivery.

2. Experimental

Materials.

Iron(II) chloride tetrahydrate ($FeCl_2 \cdot 4H_2O$, 99–102%) (Merck), trisodium citrate (100%, J. T. Baker), benzene-1,3,5-tri-carboxylic acid (trimesic acid (TMA), 98%) (Alfa Aesar), hydrazine monohydrate ($N_2H_4 \bullet H_2O$, 98%) (Alfa Aesar), fluorescein 5-isothiocyanate (Sigma-Aldrich, ~ 98%), dimethyl sulfoxide (Sigma, > 99.5%), amine-QD_{655} (Invitrogen, Life Technologies) N-(3-dimethylaminopropyl)-N'-ethylcarbodiimide hydrochloride (EDC) (Fluka), N-hydroxysuccinimide (NHS) (Aldrich), and blue tetrazolium bromide (MTT assay reagent) (AlfaAesar L11939) were purchased for use without further purification.

Rhodamine-based chemosensor to Fe ions was provided by Prof. Shu-Pao Wu at National Chiao Tung University (Taiwan). Sample was prepared according to the previous synthesis method.[25]

Preparation of Fe_3O_4 cluster-structured nanoparticles (CNPs)

The NIR-activated Fe_3O_4 CNPs were prepared by a one-pot hydrothermal reaction that was well-developed for sub-gram level preparations. Briefly, $FeCl_2 \cdot 4H_2O$ (10 mL, 50 mM), trimesic acid (TMA) (4.5 mL, 25 mM), NaOH (18 mg), trisodium citrate (0.15 g), and N_2H_4 (0.1 mL) were mixed by stirring and then immediately transferred to a 23-mL Teflon-lined stainless steel autoclave to be heated at 200 °C for 13 h. A repeated centrifugation/washing process with deionized water was employed to purify the as-synthesized Fe_3O_4 CNPs. After the purification, the as-prepared Fe_3O_4 CNPs were subjected to various analyses and stored at 4 °C until use.

Preparation of a dilution of coating of Fe_3O_4 CNPs onto calcium oxalate dehydrate (COD) crystal

Thirty-two milliliters of $CaCl_2$ aqueous solution (0.2 M) was mixed with 400 mL of trisodium citrate aqueous solution (10 mM) under 100 rpm-stirring at 23 °C. This mixture of solutions was subsequently reacted with 16 mL of sodium oxalate (0.05 M). After 15 min of reaction time, the white precipitates were collected with a 5 μm filter paper and rinsed with deionized water several times.

To prepare the SEM sample with a dilution of coating of Fe_3O_4 CNPs, 4 μL of Fe_3O_4 CNPs (4000 ppm) was added to 1 mL of the Ca-based solution (1 mg/mL). After 30 s of mixing time, the Fe_3O_4 CNP-bonded COD crystals were separated after 10 s of magnetic attraction with a magnet. Finally, the collected products were transferred onto a Cu substrate and dried under air.

Preparation of FITC-absorbed Fe_3O_4 CNPs.

20 mM of fresh FITC in DMSO solution was prepared prior to be used. Pure water was then added to dilute the FITC solution, leading to final concentration at 0.5 mM. Subsequently, 400 μL of Fe_3O_4 CNPs (250 $ppm_{[Fe]}$) was mixed with 12 μL of FITC solution (0.5 mM) overnight. The resulting FITC-absorbed Fe_3O_4 CNPs was purified by a repeated centrifugation/washing process with deionized water. The fluorescent signal of FITC (excitation at 450 nm and emission at 515 nm) from the first collected supernatant was recorded using a fluorescence spectrophotometer to calculate the difference between the initial amount of FITC and the residue in the supernatants. Less 5% of the release of FITC molecules from FITC-absorbed Fe_3O_4 CNPs was determined after 14 days (Figure S1).

Preparation of amine-QD_{655}-conjugated Fe_3O_4 CNPs.

A mixture of Fe_3O_4 CNPs (100 ppm), amine-QD_{655}, EDC (3 mg), and NHS (3 mg) was prepare at 4 ^oC for overnight to synthesize QD_{655}-conjugated Fe_3O_4 CNPs. A repeated centrifugation/washing process with deionized water was employed to purify the conjugated sample.

Nuclear magnetic relaxation dispersion profiles.

The transverse (R2) relaxation of different Fe_3O_4 CNPs suspension at 37 ^oC was recorded at 1.41 T obtained on Minispec Mq 60 spin analyzers (Bruker, Karlsruhe, Germany).

OCT imaging

OCT imaging was carried out using a spectral domain OCT (SDOCT) set-up. The design of our OCT imaging system is shown in Supporting Information, Figure S7. The light source is a supercontinuum laser with a median wavelength of 860 nm and a spectral bandwidth of 180 nm after passing through a dichroic mirror and a color filter. The system resolutions in tissue were ~2.6 μm axially and ~6 μm laterally. The system was constructed using a fiber optic Michelson interferometer with a coupler arranged to split light power into 10% for the reference mirror, and 90% incident power (i.e., approximately 10 mW) focused to a spot of approximately 6 μm in diameter. The focused sample beam was scanned by a two-axis galvanoscanner mirror. After the recombination of the sample and reference beams, the dispersed spectra, which output from the coupler and circulator, were formed and transferred to a computer via a transmission grating and a 4096 element line scan camera. The full axial image can be retrieved through a Fourier transform of the spectral interferogram. In our setup, the line scan sensors could operate in the shortest integration time (25 μs), achieving a high imaging speed of up to 40 frames per second with an image size of 1000 × 2048 pixels.

Quantitative analysis

Quantitative calculation was performed using an algorithm written in Matlab to automatically analyze the mean signal intensity per pixel and the total number of pixels with the intensity larger than 10% of the maximum. First, regions of interest (ROIs) composed of 400 x 250 pixels at the same depth from the surface were selected from each OCT image in Figure 4, 6 and S13. Then, a binary map was obtained by using a threshold (i.e., the pixel intensity under 10% of the maximum is considered as black, others are white). The summation of the white pixels in each binary map provides the occupation area of the scatterers. After the product of the binary map and the original image, the summation of pixel values normalized to the occupation area of the scatterers provides the mean intensity per pixel.

***In vitro* cell toxicity test**

HeLa cells were cultured in DMEM-HG culture medium. Cell culture began with a cell seeding density of approximately 3 x 10^4 cells/cm^2 on a 10 cm culture dish at 37°C, 5% CO_2. After 24 h, serial dilutions of loaded Fe_3O_4 CNPs samples (0-500 $ppm_{[Fe]}$) in the DMEM medium were added to the culture wells to replace the original culture medium. Subsequently, the cells were incubated with the Fe_3O_4 CNP samples for another 24 h. The culture medium was then removed and replaced with 100 μL of fresh culture medium containing 10% MTT reagent. The resulting cells were incubated at 37 °C for 4 h to allow the formation of formazan dye. The cultural medium in each well was centrifuged and collected and then transferred to an ELISA plate. The quantification of cell viability was performed using an ELISA plate reader at an optical absorbance of 540/650 nm.

Temperature examination under 808 nm laser irradiation

The temperature elevation of the Fe_3O_4 CNPs was measured by placing the material solutions (375 $ppm_{[Fe]}$) in 96-well plates and irradiating them using an 1064 nm continuous-wave (CW) diode laser and an 808 nm CW diode laser. A thermocouple was immersed in the material solutions to determine the temperature. The CW laser had a power density of 380 mW/cm^2. For the infrared thermographic map examinations, 1 mL of the Fe_3O_4 CNPs solution (375 ppm) in a 1.5 mL centrifuge tube was reacted with a 1064 nm light at a power density of 380 mW/cm^2. The thermal images of these solutions were

monitored from 0 min to 10 min using a thermographic camera (Fluke / FLK-TI32 9HZ).

OCT imaging for contrast enhancement of HeLa cancer cells treated with Fe_3O_4 CNPs

The HeLa cancer cells were cultured in 6-well plates with DMEM and maintained in an incubator under a 5% CO_2 atmosphere at 37 °C. Each well contained 2.4 x 10^5 cells for a culture time of 24 h. Three milliliters of Fe_3O_4 CNPs (150 ppm) was added to the cells and incubated for 4 h at 37 °C. To remove the unbound nanoparticles, the wells were rinsed with PBS buffer. The particle-treated cells were then cultured with trypsin-EDTA for 4 min at 37 °C to detach the cells from the culture dish. The suspended cells were counted using a hemocytometer. ~2.4 x 10^5 of cells were prepared by a re-dispersion of concentrated cells into PBS buffer solution for the OCT imaging analysis.

To determine the concentration of Fe ions, the Fe_3O_4 CNP-treated cells were dissolved by adding 4 M-HCl solution, the resulting acidic solution was then subjected to ICP-AES measurement. A control experiment was carried by aging Fe_3O_4 CNPs solution (150 $ppm_{[Fe]}$) in the culture dish for 30 min and 4 h. In each dish, we carefully removed the suspended solution and washed by PBS solution more than twice. Finally, 4 M-HCl solution was added to dissolve the residual Fe_3O_4 CNPs and then the iron concentrations was measured using ICP-AES. The non-specific absorption of Fe_3O_4 CNPs on the culture dish is less than 0.5 ppm.

To perform magnetic guided OCT imaging, the Fe_3O_4 CNP-treated cells under a magnetic attraction were continuously monitored within 32 seconds by using an OCT imaging system operated at 26 frames per second.

Laser confocal microscopes of HeLa cells with FITC-absorbed Fe_3O_4 CNPs and QD_{655}-conjugated Fe_3O_4 CNPs.

HeLa cells (2 x 10^4 cells per well) were seeded onto an eight-well chamber slides. After overnight incubation (37 °C, 5% CO2), the medium was carefully aspirated and individually replaced with 200 μL of a new medium containing FITC-absorbed Fe_3O_4 CNPs (100 $ppm_{[Fe]}$) and QD_{655}-conjugated Fe_3O_4 CNPs (100 $ppm_{[Fe]}$). After incubating for 0.5 h and 4 h, all medium were carefully removed and rinsed twice with 300 μL of PBS. The nucleus was counter-stained using DAPI (blue). Subsequently, sample slices were observed by using a confocal laser scanning microscopy (Olympus FluoView 1000 confocal laser scanning microscope, Japan) to capture DAPI, FITC, QD_{655} fluorescent images at 405 nm, 540 nm, and 655 nmrespectively. The FITC alone (0.75 μM) group was also carried out for comparison.

Rhodamine-based chemosensor to assess the Fe_3O_4 CNPs uptake.

The HeLa cells cultured in DMEM were treated with 100 $ppm_{[Fe]}$ solutions of Fe_3O_4 CNPs and incubated at 37 ^oC for 4 h. The treated cells were washed with PBS solution to remove remaining Fe_3O_4 CNP. DMEM including 0.1 M-HCl solution (1 h) was added to particle-treated cells to dissolve the Fe_3O_4 CNPs and generate Fe ions. Subsequently, DMEM-including chemosensor (20 μM) was added to the cell culture. The samples were incubated at 37 ^oC for 60 min. The culture medium was then removed, and the treated cells were washed with PBS before observation. Fluorescence imaging was performed with a confocal laser scanning microscopy. Cells loaded with rhodamine-based chemosensor were excited at 545 nm by using a Hg lamp. An emission filter of 570 nm was recorded.

Photothermal therapy of HeLa cancer cells

HeLa cancer cells were cultured in 96-well plates with DMEM and maintained in an incubator under a 5% CO_2 atmosphere at 37 °C. Each well contained 8000 cells for a culture time of 24 h, and 0.1 mL of Fe_3O_4 CNPs (375 ppm) was added to the cells and incubated for 4 h at 37 °C. To remove the unbound nanoparticles, the wells were rinsed with PBS buffer, and then fresh DMEM medium was added to each well. The photothermal killing of the cancer cells was performed using a CW diode laser with a wavelength of 1064 nm (380 mW/cm^2) for 10 min. After laser irradiation, another 24 h incubation was performed. We utilized MTT assays to examine the cell viability. Briefly, the original culture medium was removed and replaced with 100 μL of new culture medium containing the 10% MTT reagent. To yield formazan dye, the cells were incubated for 4 h at 37°C. The culture medium in each well was then removed. Dimethyl sulfoxide (DMSO) (200 μL) was added to each well, and the cells were incubated for an additional 10 min. Finally, the resulting formazan in each well was transferred to an ELISA plate after centrifugation. Quantification analysis was performed using a scanning multiwell ELISA reader at 485 nm (SpectraMax® M2^e, Molecular Devices, USA) to determine the cell viability.

To perform magnetic targeted photothermal therapy of the HeLa cancer cells, 0.1 mL of Fe_3O_4 CNPs (375 ppm) was added to the seeded HeLa cells (8000), and a magnet was then immediately placed below the 96-well for 1 min. The unbound nanoparticles were removed with PBS buffer, and fresh DMEM medium was added to each well. Subsequently, a 1064 nm CW diode laser (380 mW/cm^2) was applied to these particle-treated cells for 10 min. The particle-treated cells were further incubated for 1 day. Particle-free cells were treated with magnetic attraction plus laser irradiation as a control experiment. The cell viability was finally examined with the MTT assay as described above.

Characterization: Electron micrographs were obtained using transmission electron microscopes (TEM) at 80 kV (JEM-2000EXII), high resolution TEM at 300 kV (JEOL 3010), and a field emission scanning electron microscope (SEM) at 10 kV (XL-40 FEG; Philips). The absorption spectra of Fe_3O_4 nanoclusters were measured using a UV-vis spectrophotometer (8452A; Hewlett-Packard Company, Palo Alto, CA). The Fe ion concentration of all samples was quantified using an inductively coupled plasma atomic emission spectrometer (ICP-AES, JY138 Spectroanalyzer; Horiba Jobin Yvon, Inc., Edison, NJ). The Raman spectra of samples were obtained with a 50 × objective lens using a home-built Raman microscope equipped with a 632.8-nm air-cooled He-Ne laser as the exciting source. A thin film X-ray diffractometer (XRD) (Bruker AXS Gmbh, Karlsruhe, Germany) was utilized to analyze the crystallization of the Fe_3O_4 nanoclusters. M-H magnetization curves at 300 K were measured for the Fe_3O_4 nanoclusters using a magnetometer (MPMS-7 SQUID; Quantum Design, Inc., San Diego, CA). The X-ray photoelectron spectra (XPS) (VG Scientific 210) of the Fe_3O_4 nanoclusters were recorded using an Mg Kα source (12 kV and 10 mA). The binding energy scale was calibrated to 284.6 eV for the main (C ls) peak.

3. Results and discussion

Figure 1a presents XRD measurements of the resultant CNPs (13 h-sample). The corresponding reflection peaks were close to those of Fe_3O_4 crystals according to JPCDS card number 85-1436. Figures 1b and 1c show the scanning electron microscope (SEM) and transmission electron microscope (TEM) images, respectively, of as-obtained CNPs, which were aggregated with several Fe_3O_4 CNPs. A dilution of Fe_3O_4 CNPs was prepared and coated onto the surface of calcium oxalate dihydrate crystal (Figure 1b), representing a dispersed aggregate of Fe_3O_4 CNPs to be ~200 nm based on the SEM image estimating over 100 nanoparticles.

High-resolution TEM imaging (Figure 1d**)** further determined the high crystallization behavior of the Fe_3O_4 CNPs, where the 0.192 nm and 0.205 nm lattice spaces correspond to the (331) and (400)

planes, respectively, of the Fe_3O_4 material. These primary particles were estimated as ~21 nm with cube-like shapes. The FT-IR spectrum and XPS analyses (Figure S2) were utilized to characterize the surface of Fe_3O_4 CNPs coordinated with the citrate and TMA molecules to form Fe–carboxylate surface complexes according to the literatures.[11,26-28]

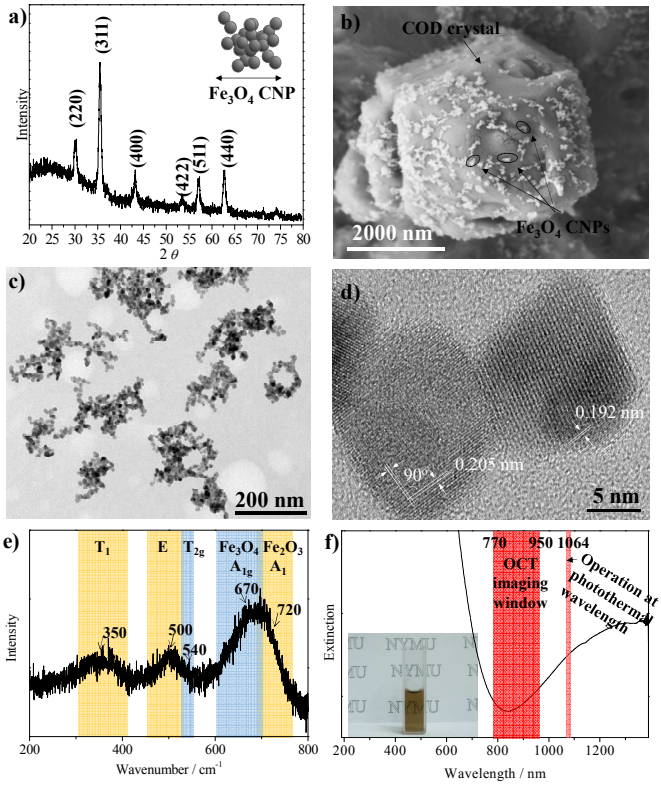

Figure 1. a) XRD pattern, b) SEM, c) TEM, d) HR-TEM, **e**) Raman spectrum, and f) UV-visible spectrum of as-prepared Fe_3O_4 CNPs (13 h-sample). SEM image of as-prepared Fe_3O_4 CNPs attached onto a single calcium oxalate dihydrate crystal. The insets in a) and f) show a cartoon picture of a single Fe_3O_4 CNP and photograph of as-prepared Fe_3O_4 CNP solution, respectively.

Figure 1e shows the Raman analysis for the as-prepared Fe_3O_4 CNPs with light excitation at 785 nm and 10 s. A dominant peak appeared at ~670 cm^{-1} (A_{1g} model) model[29] and provided strong evidence for the generation of pure magnetite (i.e., stoichiometric $[Fe^{3+}][Fe^{2+}Fe^{3+}]O_4$ structure) in the structure of the CNPs. Additionally, there are three broad humps obtained at 720 cm^{-1}, 500 cm^{-1} and 350 cm^{-1} that could be ascribed to the A_1, E, and T_1 modes, respectively, from the maghemite structure.[30] It is important to mention that these peaks at the A_{1g} and T_{2g} model positions would shrink if the magnetite portion was absent or partially oxidized.[5] The oxygen defects and rich Fe(III) ions at O_h sites in the spinel structure caused the loss of the IVCT transition.[29,30] Thus, we supposed that the composite of the primary iron oxide nanocrystal consisted of a magnetite core protected by a maghemite shell (shortened to ''Fe_3O_4'').

It is well-known that magnetite possesses an intervalence charge transfer (IVCT) transition exhibiting wide absorption behavior covering from the visible to the NIR-IR region.[5,6,27] There is a specific absorption band located at NIR-II wavelengths. To confirm this, we carried out UV-visible-NIR spectrum measurements to characterize the Fe_3O_4 CNPs (Figure 1f). The result shows an absorption band over 1000 nm, indicating that the Fe_3O_4 CNPs could absorb NIR-II photons originating from the near stoichiometric Fe_3O_4 nanocore material. Notably, the absorption curve had a valley point at a wavelength range of 750-950 nm that the absorption feature of Fe_3O_4 CNPs is different from the broadening of the absorption bands by the surface state effect.[11] These ligand-capped and maghemite shell-protected Fe_3O_4 CNPs maintained their U-shaped absorption curve over 3 months of storage at 4 °C.

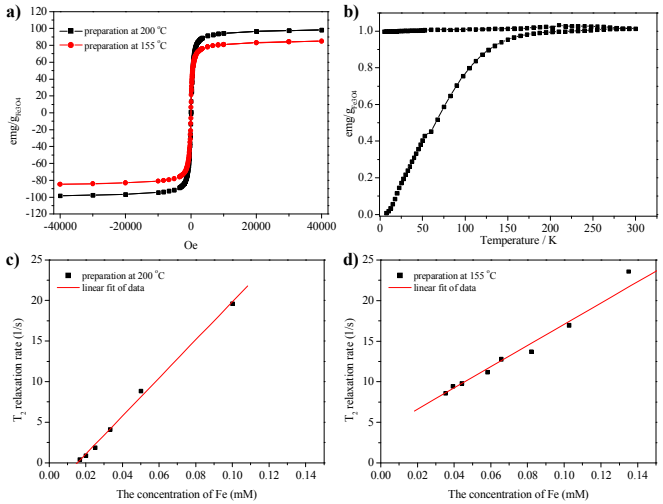

Figure 2. a) Magnetization plots at 300 K of as-prepared Fe_3O_4 CNPs prepared at 155 °C and 200 °C. b) Temperature-dependent ZFC-FC magnetization curves of as-prepared Fe_3O_4 CNPs (200 °C) measured at 100 Oe. c) and d) T_2 relaxation ($1/T_2$, s^{-1}) rate of as-prepared Fe_3O_4 prepared at 155 °C and 200 °C, respectively, as a function of iron concentrations (mM).

We employed superconducting quantum interference device (SQUID) magnetometry to characterize the magnetic properties of the Fe_3O_4 CNPs. By magnetization-magnetic field (M-H) plots at 300 K, the Fe_3O_4 CNPs show a steep slope and a lack of a hysteresis loop, indicating superparamagnetic behavior (Figure 2a). The saturation magnetization (M_s) was estimated as high as 98.3 emu/$g_{[Fe3O4]}$ and 136 emu/$g_{[Fe]}$, slightly higher than bulk Fe_3O_4 (92 emu/g). Following temperature-dependent magnetization ZFC-FC curves between 5 and 300 K at a 100 Oe (Figure 2b), the plots exhibited a broadened band, in contrast to the free-standing Fe_3O_4 nanoparticles.[31,32] The existence of strong coupling ZFC-FC curves could be attributed to the strong dipolar interactions between each Fe_3O_4 nanocrystal in a single nanocluster.

Xue and co-workers demonstrated the controlled loading of superparamagnetic nanoparticles in polymer gel led to increase the M_s with the amount of nanoparticle number much.[31] Our current result showed similar increment of M_s when the hydrodynamic radius of gelatin-coated Fe_3O_4 CNPs grown.[33] According to previous reports and our ZFC-FC result (Figure 2b), we suggested this large M_s value of Fe_3O_4 CNPs could be ascribed to the increase magnetic interparticle interactions due to the formation of Fe_3O_4 cluster form.[31-33] With additional experiments by introducing foreign gelatin containments in the same synthesis conductions, the gelatin-coated Fe_4O_4 CNPs have low M_s values of 87 emu/$g_{[Fe3O4]}$ (4 mg gelatin), 81 emu/$g_{[Fe3O4]}$ (15 mg gelatin), 73 emu/$g_{[Fe3O4]}$ (40 mg gelatin) (Figure S3). This M_s decrease trendy is likely due to the generation of the amorphous phase (spin canting)[34] at the surface layer of Fe_4O_4 CNPs in contrast to the current result of gelatin-free Fe_4O_4 CNPs (black curve in Figure 2a). In fact, the explanation of surface effects inducing the M_s reduction of Fe_4O_4 CNPs still required further investigation and was not fully understood at this stage.

Measuring transverse (T_2^{-1}) proton relaxation rates at various concentrations of iron ions, the proton relaxivity r_2 was determined as 234.6 $mM^{-1}s^{-1}$ (Figure 2c). Fe_3O_4 CNPs prepared with the same reagents at 155°C resulted in a low r_2 value at 134.7 $mM^{-1}s^{-1}$, which could be ascribed to the lower magnetization (84.8 emu/$g_{[Fe]}$). Notably, this T_2 effect of Fe_3O_4 CNPs at 234.6 $mM^{-1}s^{-1}$ is greater than most of the iron oxides nanoparticles prepared by using similar hydrothermal reaction,[9] showing Fe_3O_4 CNP as a potential contrast agent for MRI signal enhancement.

Compared to our previous synthesis method without N_2H_4,[11,27] the addition of N_2H_4 reagent significantly hindered the growth of primary Fe_3O_4 nanoparticles through aggregation and close packing. A time-dependent study demonstrated that the rapid formation of Fe_3O_4 particles consisted of several nuclei at 2 h. As the reaction was prolonged, the particle size was only slightly increased from ~16 nm (2 h) to 18 nm (6 h) to ~20 nm (12 h) to ~21 nm (13 h) (Figure 1 (13 h-sample) and Figure S4a). Accordingly, the XRD pattern (Figure S4b) determined that the reflection peak became sharper, corresponding to better crystallization, as the reaction time

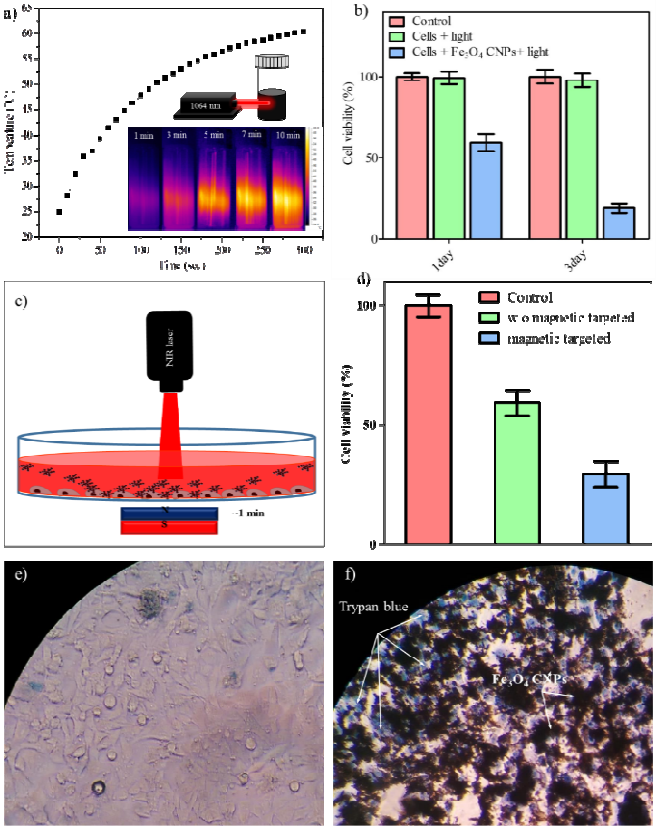

Figure 3. a) Temperature dependence of the Fe_3O_4 CNPs (375 ppm) as a function of laser irradiation time. The inset shows infrared thermographic maps of the Fe_3O_4 CNPs (375 ppm) irradiated by a dose of 0.38 W/cm^2 captured with a thermographic camera b) MTT assay after incubation periods of 1 day and 3 days to measure the viability of HeLa cells co-cultured with Fe_3O_4 CNPs for 4 h and then irradiated with a 1064 nm laser at a power density of 389 mW/cm^2 for 10 min. c) Scheme illustrating the magnetic targeted photothermal therapy of HeLa cells with Fe_3O_4 CNPs. d) MTT assay of another 1 day incubation periods for cell viability of HeLa cells co-cultured with Fe_3O_4 CNPs with 1 min of magnetic attachment and followed by irradiation using an 1064 nm laser at a power density of 380 mW/cm^2 (10 min). e) Control and f) magnetism-enhanced photothermal ablated cells by are stained with Trypan blue.

increased. When the crystallization of Fe_3O_4 CNPs was improved, the magnetization was favored to increase (Figure S4c) because of the growth of the magnetic core. Figure S4d shows the UV-visible spectra for the growth of Fe_3O_4 CNPs. The absorption band in the NIR-II regime appeared at an early stage in the reaction (2 h). The appearance of this specific optical property indicated the generation of Fe_3O_4 nuclei. Another observation was a red-shifting in the valley points as the reaction proceeded. This might be associated with particle crystallization, which must still be studied in the future.

In recent years, low-energy laser therapy (LLLT) has become an increasingly mainstream modality using an NIR laser device for curing disease.[35] For tumor depletion, the power density commonly required is 1-6 W/cm^2, despite the high penetration of NIR light.[1] To develop low power density photothermal therapy and to prevent undesired thermal side effects, we found that the absorption behavior of Fe_3O_4 CNPs in the NIR-II region exhibited promising and potent photothermal applications by using 1064 nm irradiation. Exploiting the increased NIR absorption, we excited the Fe_3O_4 CNPs (375 $ppm_{[Fe]}$) with a 1064 nm laser (380 mW/cm^2 intensity), and a thermal camera was utilized to record the water temperature as a function of time (Figure 3a). A remarkable photon-to-thermal conversion was observed from 25 °C to 59 °C in the water temperature using the NIR-II wavelength rather than NIR-I laser excitation (Figure S5).

Compared with the Fe_3O_4 sample at 155 °C (Figure S6), the 1064 nm-irradiation induced significant temperature changes by Fe_3O_4 CNPs at 200 °C at the same optical density value. It is worth mentioning that the Fe_3O_4 CNPs performed fast heating capability locally, as shown in the inset of Figure 3a, when the particles enter the area of laser irradiation. This fast photothermal conversion efficiency[36,37] of Fe_3O_4 CNPs was estimated up to 20.8 % as the time reached to 90% of the highest temperature. Indeed, the current Fe_3O_4 CNP is competitive with the available data from CdTe QDs (> 14 %),[36] free indocyanine green (15.1%)[37] and Fe_3O_4@$Cu_{2-x}S$ NPs (16 %),[38] and is also compatible to that polypyrrole-coated Au metalballs (24 %),[39] Cu_9S_5 NPs (25.7 %),[40]and Au nanorods (27%).[41]

As a result of the excellent biocompatibility (Figure S7), we then moved one step further toward cellular testing. An *in vitro* study of HeLa cell incubation with 375 ppm of Fe_3O_4 CNPs for 4 h followed by laser light excitation was performed. After 1064 nm laser treatment, the particle-treated cells were incubated for another 24 h, and the MTT assay was performed again to determine the consequent cell viability (Figure 3b). As the incubation time of the Fe_3O_4 CNPs and the cells increased, the non-viability began to decrease from 59% at 1 day to 18% at 3 days. The increment in killing cancer cells was suggested, attributed to the continuous and complex cell death pathways, e.g., apoptosis, after photothermal therapy treatment.

We next investigated the combination of magnetic targeting over a very short time (~1 min) to rapidly concentrate the Fe_3O_4 CNPs onto the HeLa cell surface and then them exposed to 1064 nm laser light (Figure 3c). A MTT assay showed ~ 65% cell death after a further 24 h of incubation time (Figure 3d). Cell viability results showed that the photothermal ablation of HeLa cells was consequently improved in contrast to a magnetic field-free cell culture situation over a short period of time. Trypan blue was used to stain the control cells (Figure 3e) and particle-treated cells (Figure 3f). It was observed that Fe_3O_4 CNP-targeted cells took on a blue color.

To demonstrate if Fe_3O_4 CNPs could serve as a useful OCT contrast agent for tumor cell imaging, we imaged one chamber containing 2.4 x 10^5 HeLa cells (Figure 4a), another chamber to which 150 ppm Fe_3O_4 CNPs were added into seeding cells after 30 minutes of incubation time (Figure 4b), and a third after 4 h of

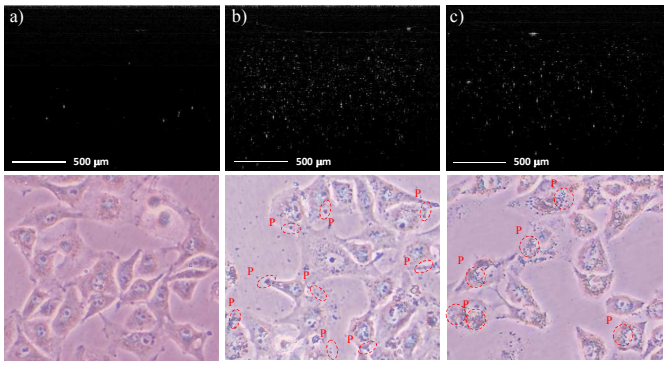

Figure 4. OCT images (top views) and bright field images (bottom views) for a) HeLa alone, b) HeLa cells plus Fe_3O_4 CNPs (150 $ppm_{[Fe]}$) after 30 minutes, and c) HeLa cells plus Fe_3O_4 CNPs after 4 hours.

incubation time (Figure 4c) using the OCT system (Figure S8). The addition of Fe_3O_4 CNPs to the cells strengthened the scattering signals (bright spots) compared to the chamber with cells alone. The quantitative analysis (Figure S9a) showed a significant increase in the number of bright spots when the cells were treated with Fe_3O_4 CNPs, as determined by the number of pixels. Mean intensity per pixel was nearly the same in the 30 min and 4 h (Figure S9b). To understand the cell-particle interactions, the corresponding bright field images are also shown on the bottom of the OCT images in Figure 4a-c. The circles and P symbols indicate the locations of Fe_3O_4 CNPs in the cells. Clearly, Fe_3O_4 CNPs initially attached to the surface of the cells and then were gradually internalized into the cell body according to the bright field observation.

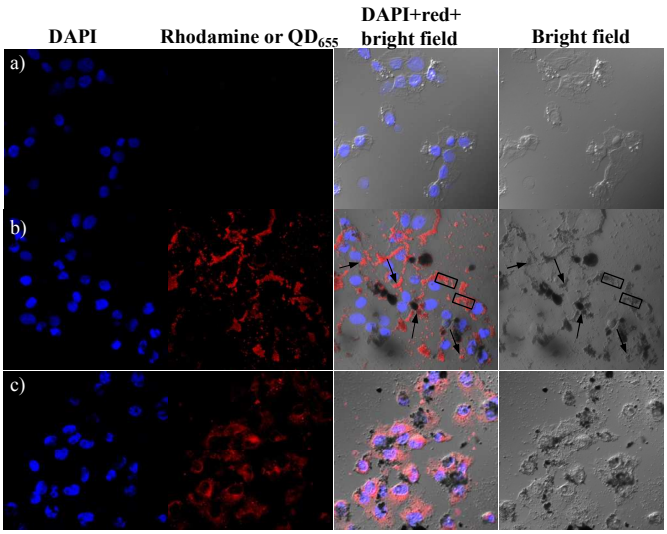

Figure 5. Confocal images of HeLa cells after different treatments: a) cell alone (4 h), b) QD_{655}-conjugated Fe_3O_4 CNPs (4h), and c) Fe_3O_4 CNPs (4 h) + rhodamine-based chemosensor/HCl. Particles attached to the surface of cells and taken into cells are labelled with squares and arrows, respectively.

Confocal laser image (Figure S10) validated the uptake of FITC-absorbed Fe_3O_4 CNPs appeared as discrete dots within the cytoplasm after 4 h of incubation. This result is distinct from the diffusion pattern of free FITC fluorophores in the cytoplasm (Figure S11). To eliminate the interference of the un-desired FITC release from FITC-absorbed Fe_3O_4 CNPs, we conducted QD_{655}-conjugated Fe_3O_4 CNPs and incubate with HeLa cells (4 h). Indeed, confocal images show superimposed fluorescent of the red emission from the QD_{655} and dark color dots from the Fe_3O_4 CNPs (bright field image) are shown superimposed (Figure 5b). They are distributed inside the cell body (labelled with arrows) as well as on the surface of cells (labelled with squares). A clear image was also provided in Figure S12. Figure 5a shows a cell alone control experiment. Next, we utilized rhodamine-based chemosensor[25] to directly prove that Fe_3O_4 CNPs resided in the cytoplasm of HeLa cells. As the addition of HCl (0.1 M) to dissociate the Fe_3O_4 CNPs-treated HeLa cells (after 4 h-incubation time), the leakage of Fe ions in the interior of cells was captured and stained with rhodamine-based chemosensor,[25] giving rise to red fluorescence (Figure 5c). Despite the fact that the larger Fe_3O_4 residuals primarily localize around the cell surface, the red color emission represented fluorescently labelled Fe ions which spread throughout the cytoplasm. The result suggested that only the internal Fe ions could be reacted with rhodamine-based chemosenso after acid-induced dissociation of the embedded Fe_3O_4 CNPs. A simple washing process could rapidly remove the Fe ions from the HCl-treated Fe_3O_4 CNPs outside living cells.

We carried out ICP-AES measurements and found that the concentrations of Fe_3O_4 CNPs into/onto the cells at 30 min and 4 h were ~20 ppm and 25 ppm, respectively. A control experiment on a dispersion of Fe_3O_4 CNPs alone (25 ppm) did not produce remarkable scattering signals (Figure 4a), and the number of pixels was less than that of the cell-particle complex (Figure S9a). Therefore, we supposed that the clustering effect of Fe_3O_4 CNPs attached to and/or taken into HeLa cells gave rise to not only the reflection signal enhancement but also the greater mean signal intensity per pixel.

By placing a magnetic bar on the bottom of the chamber, a magnetic attachment was implemented for the vertical movement of the Fe_3O_4 CNP-treated HeLa cells (2.4×10^5) and their ultimate deposition on the bottom of the chamber. As shown in the video in Supporting Inform ation (Video S1), the positional changes of the cells over time took on a meteor shower like trajectory toward the magnet target. This indicates that using a magnetic operation can further control these cells after their uptake of Fe_3O_4 CNPs (i.e., compared to no movement of the cell alone sample in Supporting Information Video S2).

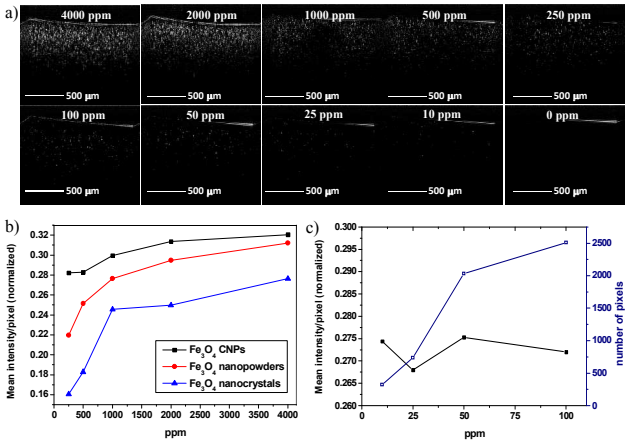

Figure 6. a) X–Z images from a chamber containing different concentrations of Fe_3O_4 CNPs in water solutions using UHR-OCT operating at a center wavelength of 860 nm. b) Quantitative analysis of the contrast enhancement by using different forms of Fe_3O_4 nanocrystals. c) Quantitative analysis of the mean signal intensity per pixel of Fe_3O_4 CNPs

Taking an advantage of the distinct U-shaped absorption curve of Fe_3O_4 CNPs, the minimal absorption at NIR-I avoids the consumption of 860 nm-laser light irradiation as well as minimizing

thermal side effects (Figure S5). OCT laser systems at shorter NIR-I wavelength regions (650-950 nm) provide higher axial resolution and also deliver more contrast in comparison to the longer wavelength regions.[7] The solid Fe_3O_4 CNPs changed the local reflection index in contrast to the liquid medium that the difference in the refractive index between the Fe_3O_4 CNPs and the water resulted in a strong scattering effect, which offer contrast enhancement in an OCT system. Figure 6a shows the evaluation of OCT imaging contrast enhancement of Fe_3O_4 CNPs with concentrations of 0-4000 ppm. We calculated the mean signal intensity per pixel in Figure 6b to quantitatively compare the contrast enhancement. The addition of Fe_3O_4 CNPs produced more intense scattering signals, even below a concentration of 1000 ppm. Compared to a water solution alone (i.e., Fe_3O_4 CNPs with concentrations of 0 ppm), only the air-water interface can be seen clearly.

Parallel experiments using commercial Fe_3O_4 nanopowder (Alfa Aesar, 20-30 nm) and non-cluster structured Fe_3O_4 nanocrystals (MagQu, 31 nm±8.33 nm) were also carried out, as shown in Figure 6b and Figure S13. For concentrations below 1000 ppm, both commercial Fe_3O_4 solutions showed a dramatic decrease in the mean signal intensity per pixel. We then analyzed the mean signal intensity per pixel and the number of pixels (with the intensity larger than 10% of the maximum) in Fe_3O_4 CNPs of very low concentrations (Figure 6c). Clearly, the number of pixels decreased with the decrease in Fe_3O_4 CNP concentration, whereas the mean signal intensity per pixel remained strong. This implies that Fe_3O_4 CNPs are highly suitable for low-dose usage because its special clustered form enhances the scattering more than the conventional nanoparticle structure.

As mentioned above, we established the magnetic properties of Fe_3O_4 CNPs offering a magnetomotive OCT image when the cell interacted with Fe_3O_4 CNPs (see Video S1 in Supporting Information). Both NIR-I OCT imaging and NIR-II photothermal therapeutic results indicated that the Fe_3O_4 CNP is a promising magnetic-guided biophotonics agent.

4. Conclusions

In conclusion, we report a ligand-assisted hydrothermal reaction to fabricate cluster-structured nanoparticles composed of several Fe_3O_4@Fe_2O_3 nanocrystals. The absorption band of Fe_3O_4@Fe_2O_3 CNPs has a valley area at the range of 750-950 nm and exhibited a progressive evolution in the NIR-II region. After the incubation of HeLa cells with Fe_3O_4 CNPs, we applied 1064 nm to excite these Fe_3O_4-cell complex samples, resulting in significant cancer cell death. By using an OCT system with an 860 nm laser, a contrast enhancement was available by using a Fe_3O_4 CNP-based OCT contrast agent to improve OCT light scattering significantly, hence facilitating the early-stage detection of small cancers. A relatively low concentration of CNPs (~25 ppm) attached to and/or internalized into HeLa cells resulted in an improvement in OCT image contrast in contrast to cells alone. Importantly, both of the imaging and therapeutic effects using Fe_3O_4 CNPs were controllable and improvable with magnetic gradient control.

Our demonstration brings new insights for the possible integration of biophotonics and Fe_3O_4 CNPs in nanomedicine as a new theranostic platform for local cancer treatment combining OCT imaging with phototherapy, i.e., the development of real-time operation and positioning of photothermal Fe_3O_4 CNPs agents in the deep tissue using OCT microscope with magnetic particle manipulation. OCT imaging guidance may also provide compensatory technology to execute magnet-assisted accumulation of Fe_3O_4 nanoparticles while overcoming the restriction of magnetic material in MRI working area. The in vivo study for a new concept of local cancer treatments through OCT imaging-phototherapy will be necessary in the next step.

Acknowledgements

This work was supported in part by grants from the National Science Council (Grant Nos. MOST 103-2113-M-010-001-MY2, NSC 102-2221-E-010-006-MY3, NSC 101-2113-M-010-002-MY2, and 102-2112-M-010-002-MY3) of Taiwan.

Notes and references

[a] Department of Photonics, Center for Micro/Nano Science and Technology, and Advanced Optoelectronic Technology Center, National Cheng Kung University, 701, Tainan, Taiwan. Email: c2huang@mail.ncku.edu.tw; huang.chihchia@gmail.com

[b] Institute of Biophotonics, National Yang-Ming University, Taipei, 112, Taiwan. Email: wckuo@ym.edu.tw

[c] Biophotonics and Molecular Imaging Research Center (BMIRC), National Yang-Ming University, Taipei, 112, Taiwan

[d] Department of Applied Chemistry, National Chiao Tung University, Hsinchu, Taiwan.

† Footnotes: DLS, FT-IR, XPS, SQUID, and MTT assay measurements of Fe_3O_4 CNPs were presented. Additional photothermal effects, quantitative analysis of HeLa cells and Fe3O4 nanoparticles with OCT microscope system.. See DOI: 10.1039/b000000x/

1 L. Cheng, C. Wang, L. Feng, K. Yang and Z. Liu, *Chem. Rev.*, 2014, **114**, 10869.
2 Z. Zhou, B. Kong, C. Yu, X. Shi, M. Wang, W. Liu, Y. Sun, Y. Zhang, H. Yang and S. Yang, *Sci. Rep.*, 2014, **4**, 3653.
3 Y. Li, T. Lin, Y. Luo, Q. Liu, W. Xiao, W. Guo, D. Lac, H. Zhang, C. Feng, S. Wachsmann-Hogiu, J. H. Walton, S. R. Cherry, D. J. Rowland, D. Kukis, C. Pan and K. S. Lam, *Nature Commun.*, 2014, **5**, 4712.
4 J. U. Menon, P. Jadeja, P. Tambe, K. Vu, B. Yuan and K. T. Nguyen, *Theranostics*, 2013, **3**, 152.
5 J. Tang, M. Myers, K. A. Bosnick, L. E. Brus *J. Phys. Chem. B*, 2003, **107**, 7501.
6 Y. P. He, Y. M. Miao, C. R. Li, S. Q. Wang, L. Cao, S. S. Xie, G. Z. Yang and B. S. Zou, *Phys. Rev. B: Condens. Matter Mater. Phys.*, 2005, **71**, 125411.
7 A. Alex, B. Pocazay, B. Hofer, S. Popov, C. Glittenberg, S. Binder and W. Drexler, *J. Biomed. Opt.*, 2010, **15**, 026025.
8 J. Park, E. Lee, N. M. Hwang, M. Kang, S. C. Kim, Y. Hwang, J. G. Park, H. J. Noh and J. Y. Kim, *Angew. Chem. Int. Ed.*, 2005, **44**, 2872.
9 J. Li, X. Shi and M. Shen, *Part. Part. Syst. Charact.*, 2014, *31*, 1223.
10 M. Chua, Y. Shao, J. Peng, X. Dai, H. Li, Q. Wu, D. Shi, *Biomaterials*, 2013, **34**, 4078.
11 M. Y. Liao, P. S. Lai, H. P. Yu, H. P. Lin and C. C. Huang, *Chem. Commun.*, 2012, **48**, 5319.
12 *H. Chen, J. Burnett, F. Zhang, J. Zhang, H. Paholak, D. Sun, J. Mater. Chem. B,* 2014, **2**, 757.

13 W. Tan, A. L. Oldenburg, J. J. Norman, T. A. Desai and S. A. Boppart, *Opt. Express*, 2006, **14**, 7159.
14 W. Hatta, K. Uno, T. Koike, K. Iijima, N. Asano, A. Imatani and T. Shimosegawa, *Gastrointest. Endosc.*, 2012, **76**, 548.
15 D. Huang, E. A. Swanson, C. P. Lin, J. S. Schuman, W. G. Stinson, W. Chang, M. R. Hee, T. Flotte, K. Gregory, C. A. Puliafito and J. G. Fujimoto, *Science*, 1991, **254**, 1178.
16 W. C. Kuo, C. M. Lai, Y. S. Huang, C. Y. Chang and Y. M. Kuo, *Opt. Express* 2013, **21**, 19280.
17 F. T. Liao, C. Y. Chang, M. T. Su and W. C. Kuo, *J. Biomed. Opt.*, 2014, **19**, 011014.
18 S. A. Boppart, A. L. Oldenburg, C. Xu and D. L. Marks, *J. Biomed. Opt.*, 2005, **10**, 041208.
19 C. Xu, J. Ye, D. L. Marks and S. A. Boppart, *Opt. Lett.*, 2004, **29**, 1647.
20 C. Yang, L. E. McGuckin, J. D. Simon, M. A. Choma, B. E. Applegate and J. A. Izatt, *Opt. Lett.*, 2004, **29**, 2016.
21 Z. Yaqoob, E. McDowell, J. Wu, X. Heng, J. Fingler and C. Yang, *J. Biomed. Opt.*, 2006, **11**, 054017.
22 J. Chen, F. Saeki, B. J. Wiley, H. Cang, M. J. Cobb , Z. Y. Li, L. Au, H. Zhang, M. B. Kimmey, Xingde and Y. Xia, *Nano Lett.*, 2005, **5**, 473.
23 T. M. Lee, A. L. Oldenburg, S. Sitafalwalla, D. L. Marks, W. Luo, F. J. J. Toublan, K. S. Suslick and S. A. Boppart, *Opt. Lett.*, 2003, **28**, 1546.
24 K. M. Au, Z. Lu, S. J. Mathcher and S. P. Armes, *Adv. Mater.*, 2011, **23**, 5792.
25 S.-R. Liu and S.-P. Wu, *Sens. Actuators B*, 2012, **171– 172**, 1110.
26 A. G. Roca, J. F. Marco, M. d. P. Morales and C. J. Serna, *J. Phys. Chem. C* **2007**, *111*, 18577.
27 M. Y. Liao, C. H. Wu, P. S. Lai, J. S. Yu, H. P. Lin, T. M. Liu and C. C. Huang, *Adv. Funct. Mater.* **2013**, *23*, 2044.
28 Y.-L. Huang, H.-W. Tien, C.-C. M. Ma, S.-Y. Yang, S.-Y. Wu, H.-Y. Liu and Y.-W. Mai, *J. Mater. Chem.* **2011**, *21*, 18236.
29 T. J. Daou, G. Pourroy, S. Bégin-Colin, J. M. Grenèche, C. Ulhaq- Bouillet, P. Legaré, P. Bernhardt, C. Leuvrey and G. Rogez, *Chem. Mater*., 2006, **18**, 4399.
30 F. Vereda, J. de Vicente, M. D. P. Morales, F. Rull and R. Hidalgo- Alvarez, *J. Phys. Chem. C*, 2008, **112**, 5843.
31 E. S. G. Choo, X. Tang, Y. Sheng, B. Shuter and J. Xue, *J. Mater. Chem.*, 2011, **21**, 2310.
32 S. M. Lai, J. K. Hsiao, H. P. Yu, C. W. Lu, C. C. Huang, M. J. Shieh and P. S. Lai, *J. Mater. Chem.*, 2012, **22**, 15160.
33 Y.-C. Chiu, P.-A. Chen, P.-Y. Chang, C.-Y. Hsu, C.-W. Tao, C.-C. Huang, and H. Chiang, *J. Mater. Chem. B*, DOI: 10.1039/c5tb00419e.
34 C. Pereira, A. M. Pereira, C. Fernandes, M. Rocha, R. Mendes, M. P. Fernández-García, A. Guedes, P. B. Tavares, J.-M. Grenèche, J. P. Araújo and C. Freire, *Chem. Mater.,*.2012, **24**, 1496.
35 J. T. Hashmi, Y. Y. Huang, B. Z. Osmani, S. K. Sharma, M. A. Naeser, M. R. Hamblin, *Pm&R*, 2010, **2**, S292.
36 M. Chua, X. Pan, D. Zhang, Q. Wu, J. Peng and W. Hai, *Biomaterials*, 2012, **33**, 7071.
37 M. Zheng, P. Zhao, Z. Luo, P. Gong, C. Zheng, P. Zhang, C. Yue, D. Gao, Y. Ma and L. Cai, *ACS Appl. Mater. Interfaces*, 2014, ***6***, 6709.
38 Q. Tian, J. Hu, Y. Zhu, R. Zou, Z. Chen, S. Yang, R. Li, Q. Su, Y. Han and X. Liu, *J. Am Chem Soc.*, 2013, **135**, 8571.
39 H. Zhang, J. Li, J.S. Han, T.S. Xu, C.R. Guo and X.Y. Bu, *Langmuir*, 2013, **29**, 7102.
40 C. M. Hessel, V. P. Pattani, M. Rasch, M. G. Panthani, B. Koo, J. W. Tunnell and B. A. Korgel, *Nano Lett.*, 2011, **11**, 2560.
41 B. Nikoobakht, J. P. Wang and M. A. El-Sayed, *Chem. Phys. Lett.*, 2002, **366**, 17.

